Available online at www.sciencedirect.com
ScienceDirect
Earth and Planetary Science Letters 257 (2007) 372–390
EPSL
www.elsevier.com/locate/epsl

The role of climate during high plateau formation. Insights from numerical experiments

Daniel Garcia-Castellanos

Institute of Earth Sciences Jaume Almera (ICTJA-CSIC), Solé i Sabarís s/n, 08028 Barcelona, Spain
Netherlands Centre for Integrated Solid Earth Science (ISES), Faculty of Earth and Life Sciences, Vrije Universiteit Amsterdam, De Boelelaan 1085, 1081HV Amsterdam, The Netherlands

Received 6 July 2006; received in revised form 5 January 2007; accepted 25 February 2007
Available online 3 March 2007
Editor: G.D. Price

Abstract

High plateaus are elevated areas of low relief mostly associated with compressional tectonics and characterized by dry climatic conditions. Results from a novel computer modeling technique integrating surface and tectonic processes suggest that a pre-existing dry climate, through its effects on surface transport and orogenic evolution, can significantly contribute to the formation of high plateaus. According to these results, dry climatic conditions promote sediment trapping within the orogen, transferring the accommodation of tectonic shortening towards the external parts of the orogen and leading to the formation of a high plateau. This feedback operates in the following steps: (1) dry climatic conditions at the early stages of orogenesis favor the tectonic defeat of rivers draining the orogen, promoting internal drainage (endorheism); (2) endorheism extends the life of intramountain basins maximizing the mass trapped within the orogen and expelling deformation further into the foreland; and (3) this propagation of deformation further isolates the central parts of the orogen from incoming precipitation, reinforcing sediment trapping and topographic leveling of the intramountain region. This phenomenon allows reproduction of basic topographic, drainage, and tectonic differences between orogens lacking a high plateau, such as the Alps, and orogens with a well-developed high plateau like the Andes, without invoking inherited heterogeneities in the crust or other tectonic processes. It also suggests that internal drainage and high plateaus might be a natural stage of orogenesis undergoing dry climatic conditions. In the light of recent data reporting dry climate prior to the formation of the Andean high plateau, aridity can be seen as one of the causes for the formation of the Altiplano, rather than just as a consequence of topographic growth.

Keywords: endorheic basin; orogen; surface processes; numerical model; Altiplano; Andes

1. Introduction. Tectonic and erosional controls on orogenesis

Continental high plateaus are elevated areas of subdued relief surrounded by mountain chains. Most investigations regard the formation of high plateaus as the result of tectonic uplift processes disrupting surface mass transport within an orogen. Thermomechanical models suggest that weakening of the lower crust favors strain partitioning and the isolation of a high plateau within an orogen [1–6]. In the case of the Andean Altiplano, crustal shortening accounts for the bulk of crustal thickening, but questions remain about whether

E-mail address: danielgc@ija.csic.es.

0012-821X/$ - see front matter © 2007 Elsevier B.V. All rights reserved.
doi:10.1016/j.epsl.2007.02.039

this deformation consists mostly of lateral viscous flow in the lower crust [7], or brittle failure by means of crustal-scale imbricated thrusts ([8,9]; see Fig. 1), and on what is the contribution of subcrustal processes to uplifting the Altiplano [10].

In this context, surface processes have been mostly seen as passively responding to these tectonic events by eroding the orogen and filling the intramountain sedimentary basin (e.g., [11]). According to these models, the lack of a high plateau in the Alps (Fig. 1), for example, would have been determined by the lack of strain partitioning in two separated cordilleras as a result of an inherited lithospheric structure different from that in the Andes. From this point of view, climate and surface transport act as mechanisms that fill the tectonic topographic lows of the orogen and flatten the endorheic internal areas leading to the formation of the high plateau, as described for the Tibet plateau by Métivier et al. [12].

However, modeling studies show that erosion has a significant feedback influence on orogen dynamics.

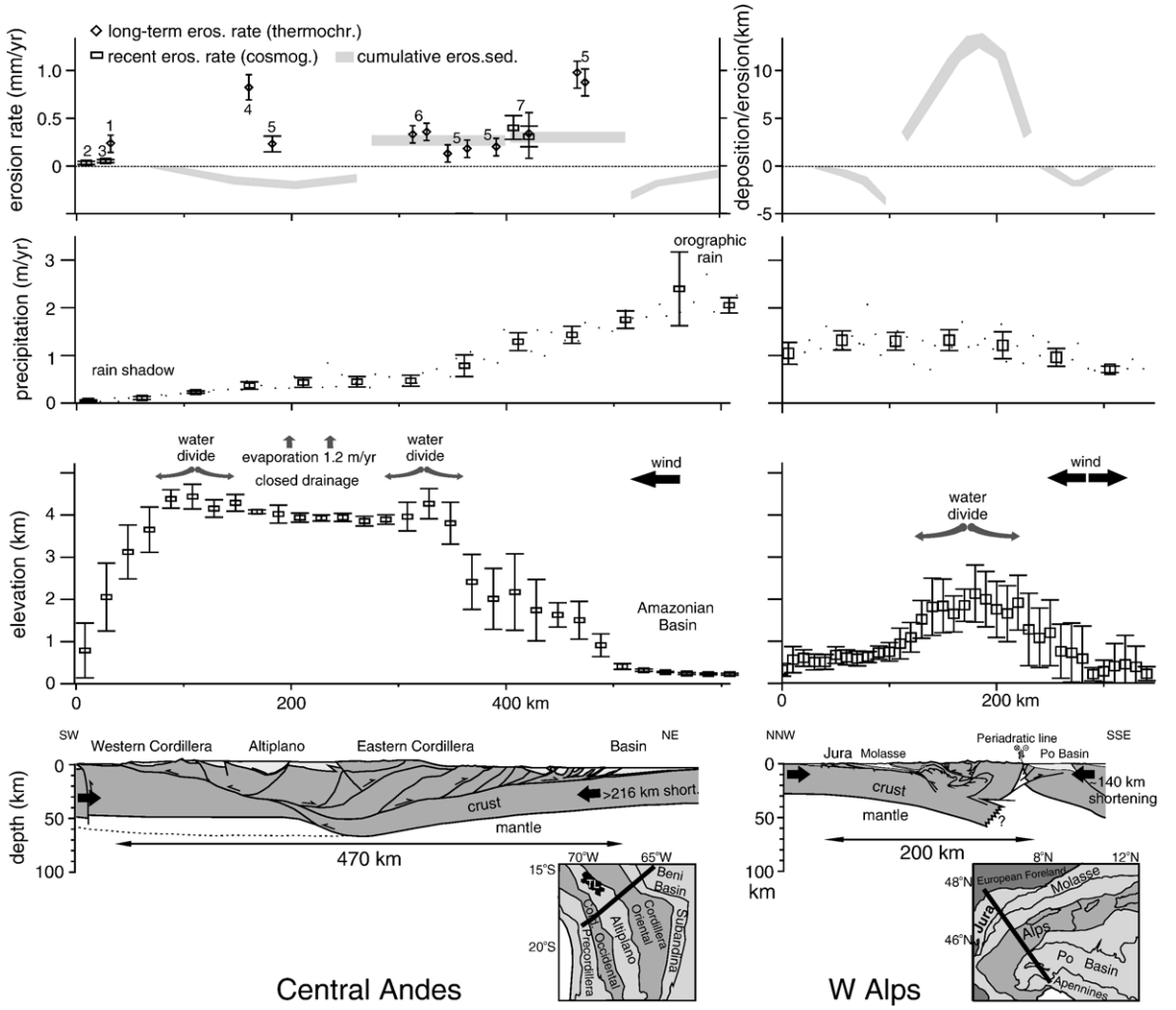

Fig. 1. Comparison of erosion, precipitation, and tectonic structural profiles across the Andes (left panels) and the Alps (right). (a) Symbols indicate long- and short-term erosion rate measurements in mm/yr (1. [53]; 2. [54]; 3. [55]; 4. [56]; 5. [57]; 6. [58]; 7. [59]); grey bands indicate cumulative erosion/sedimentation in km for the Central Andes (syn- and post-uplift, from [57]) and the Alps (post-collisional, as compiled in [34]). (b) Precipitation as compiled by the Center for Climatic Research (Univ. Delaware). (c) Topography and drainage divides. (d) Schematic structural sections (simplified from [8], and NFP20 seismic traverse). Error bars in (b) and (c) represent standard deviations within the 100 km-wide data projections, whereas in (a) they represent an estimation of measurement error. Note that data in (a) are projected along a wider region than (b) and (c), due to the scarcity of erosion data. The westwards dominant wind in the Andes induces maximum orographic precipitation in the East and a marked orographic rain shadow in the western side of the Andes (Peruvian Coast), whereas in the Alps these features are missing due to more variable wind directions. The up to 3.5 km-thick syn-orogenic sedimentation in the Altiplano contrasts with the maximum exhumation values along the axis of the Alps.

According to numerical crustal-scale simulations of orogenesis incorporating surface processes, the propagation of deformation into the forelands flanking an orogen is smaller when erosion is more efficient in removing mass from the orogen surface. In this sense, climatic parameters such as the dominant wind direction and the resultant side of the orogen receiving most precipitation appear to be important in determining the later tectonic evolution and structure of a mountain belt [13–16]. Results obtained from analogue sandbox experiments (e.g., [17,18]) show similar effects.

When comparing orogens containing a high plateau like the Andes to those lacking a plateau, such as the Alps (Fig. 1), differences are in fact as important in terms of surface transport as in terms of tectonic structure. Although exhumation data shown in Fig. 1a are still incomplete, it is clear that whereas in the center of the Bolivian Andes there is a deep syn-orogenic basin surrounded by two eroded cordilleras, in the Alps maximum erosion of up to 15 km is concentrated along the axis of the orogen. This distinct surface transport plays an active role during the development of both orogens and contributes to shape their structure [19].

Thus, important question marks remain on the origin of high plateaus: what triggers the early formation of an internally drained basin within an orogen? What is the effect of sediment trapping within the orogen on the later development of a high plateau? Are inherited tectonic structures or other tectonic processes required to explain strain partitioning and high plateau formation? Or can internal drainage and the weight of trapped intraorogenic sediments do that job on its own?

In this study, the hypothesis is tested that climate can actively modify the tectonic deformation pattern and contribute to high plateau formation by promoting intraorogenic endorheism, as suggested by recent modeling studies of intramountain basins [20,21]. First, an overview of the processes leading to drainage closure within an orogen is given. Then, a cross-sectional computer model of orogen and basin evolution is designed accounting for the interactions between four processes: (1) pseudo-dynamic propagation of tectonic deformation by thrusting; (2) orographic precipitation and evaporation, and hydrological balance; (3) surface erosion/transport/deposition of sediment; and (4) flexural isostasy. The model permits parameterizing the impact of intraorogenic sediment trapping on the lateral-vs.-vertical growth of the orogen. The model aims to explain, through changes in climatic parameters, some basic topographic and tectonic differences between orogens with high plateaus (such as the Andes) and orogens lacking a high plateau (Alps). The results are discussed in the light of recent climatic constrains on the Andes suggesting that dry climate preceded the main tectonic uplift phase.

2. Internally drained basins and high plateaus

High plateaus are in general geographically associated with internally drained basins, the most outstanding examples being the Tibetan Plateau and the Andean Altiplano (both too included among the largest internally drained basins in the world). Internally drained (endorheic) basins on high plateaus result from the isolation from incoming humid air imposed by the surrounding topography, leaving the basin in an orographic *rain shadow* that reduces the capability of rivers to excavate an outlet towards the ocean. Such drainage closure imposes a dramatic reduction in the evacuation of erosional products from the orogen. Sobel et al. [20], Garcia-Castellanos et al. [21] and Garcia-Castellanos [22] have shown using numerical modeling techniques that low precipitation and high lake evaporation are quantitatively as important as tectonic uplift in helping to form internally drained basins. Masek et al. [23] found that the orographic controls on precipitation also prolong the life of continental plateaus by eroding the escarpment flanking the plateau, which uplifts by isostatic rebound. However, although these works partially explain why plateaus and internally drained basins persist for long time periods, they do not incorporate the dynamics of continental deformation and hence they cannot evaluate feedback effects between intramountain sediment trapping and orogenesis.

In endorheic hydrological basins, collected surface water is evaporated within the basin, often in central lakes, instead of being delivered to the oceans. The occurrence, evolution, and sedimentary facies of tectonic lakes are equally influenced by climate and tectonics [24,22]. Under wet climatic conditions, lacustrine basins are ephemeral systems over geological time scales that disappear by outlet erosion and/or sediment overfill as the forming mechanism comes to an end. Unless maintained by a very active tectonism (as in Lake Baikal), long-living lake systems occur only in relatively dry, endorheic areas such as the Andean Altiplano and the Dead Sea, because endorheism inhibits outlet excavation. Intramountain basins, often presenting long lacustrine periods (e.g., [25]), become endorheic sedimentary traps depending on the balance between the collected precipitation and the evaporation at lakes. If the basin increases in altitude (e.g., by sediment accumulation), a change from endorheic to exorheic drainage (caused for example by a climatic change to wetter

conditions) activates an abrupt basin-wide incision, as reported in a diversity of geological scenarios including the Tertiary Ebro Basin in the Pyrenees [21], or the Ma'adim Vallis on Mars [26]. Soon after opening, the process of basin excavation becomes difficult to revert, because the high slope of the outlet river provides a high incision capacity. The development of high topography around the basin favors its drainage closure because it blocks the income of humid wind, but if the basin itself reaches an important altitude then closed drainage is less probable because of the high slope and high incision power of the outlet river. The dynamics of endorheic basins are key to the flow of sediment out of orogens and therefore to the effects of climate and surface processes on orogenesis. Numerical modeling techniques permit studying this process interaction.

3. Model assumptions and formulation

To simulate the process interplay at the orogen-basin scale, we require physical–mathematical approaches for the tectonic, climatic, and surface processes involved (Fig. 2). The associated mathematical equations are numerically solved in 2D (cross-section) developing a finite difference code named *tAo* substantially modified after Garcia-Castellanos et al. [27] and available at the author's web page. The algorithm operates in 7 time-iterative steps: (1) determination of active faults and the corresponding tectonic deformation; (2) determination of topographic changes related to tectonic deformation; (3) calculation of orographic precipitation along the section; (4) determination of local topographic minima (lakes); (5) determination of water discharge at every location, and the extension of lakes accounting for evaporation and possible endorheism; (6) determination of the amount of material eroded/deposited at each location; and (7) isostatic compensation of water and rock mass flow via an elastic lithospheric flexural model. Iterating these steps through time yields to the tectonic, topographic and drainage evolutions described later in this paper. The fundamentals and mathematical formulation adopted for the calculations can be found in Appendix A.

The algorithm computes the distribution of atmospheric water, precipitation and evaporation along 1441 discretization points spaced by $dx = 0.5$ km. Then water discharge is computed at every point, which allows calculating the amount of river incision, transport and sedimentation. The weight of eroded and deposited rock, and that of water accumulated in lakes and sea, is accounted for when calculating the formation of new faults and the isostatic compensation as described in Appendix A. The amount of crustal material entering the model domain matches the crustal thickening in the orogen plus the sediment accumulation plus the sediment flow at the boundaries. Similarly, the amount of vapor entering the model at the boundary equals the amount of water leaving it as vapor or as surface water, during each time step of the model evolution.

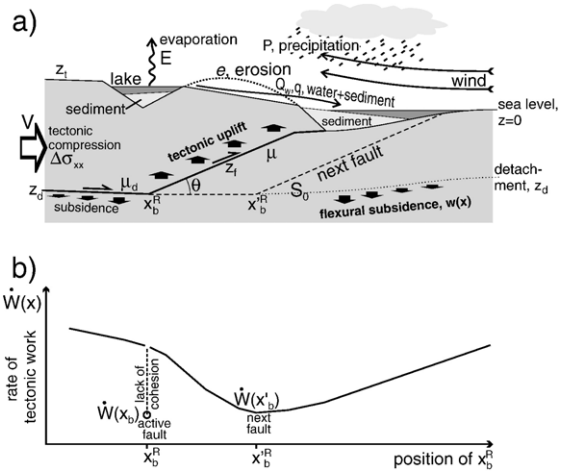

Fig. 2. Conceptual model used for the simulations (cartoon). (a) Tectonic deformation is calculated with a minimum-work criterion of fault propagation. Erosion and transport are calculated via a stream power law model of fluvial incision and transport. Water flow is calculated accounting for a simplified evaporation law and an orographic precipitation model (see Appendix A for notation and formulation). (b) Schematic diagram of rate of work as a function of the fault's x^{R}_{b} position (where the fault leaves the detachment level towards the surface) indicating the power consumed by the active fault (circle). Because cohesion S_0 is null along an active fault, this requires less work than other proximal potential faults (see Appendix A). As shortening generates topography, pressure along the fault $\rho_c g(z_t - z_f)$ increases and so does the amount of work required to accommodate the shortening rate V. Lower friction along the detachment level ($\mu_d < \mu$) ensures the eventual formation of a new fault at x'^{R}_{b} that minimizes the amount of work required, i.e., $W(x'^{R}_{b}) < W(x^{R}_{b})$. Thus, the new fault displayed in (a) forms at the point of minimum required work, x'_b in b.

A limitation that must be kept in mind comes from the power-law model adopted for river incision and transport. The ongoing research on the appropriate equations describing this process (e.g., [28–30]) relies on poorly constrained parameters that depend on lithology, vegetation, climate episodicity, etc., and hence lacks a true prediction capability. This, together with the cross-section character of the modeling, limits the interpretation of the results to the qualitative interaction between processes, rather than reproducing data from a particular scenario. Similarly, though simplistic approaches are also adopted to simulate tectonic deformation, the reliability of the interactions identified in the next sections is ensured by the reasonable amounts of erosion and deposition produced

in the simulations, and the reasonable widths and altitudes of the simulated orogens relative to those in nature.

4. Input parameters

For the sake of simplicity (i.e., to facilitate the interpretation of model results and of interactions between the 4 processes involved), the model setup is kept as schematic as possible. The initial topography of the model is assumed to be flat at sea level ($z=0$; Fig. 1). It is also assumed that 2 initial thrusts of opposite vergence accommodate the imposed shortening rate, defining an initial pop-up structure. The thrusting units defined on the left side ($x<0$) are structurally higher than those on the right side ($x>0$; see Fig. 3).

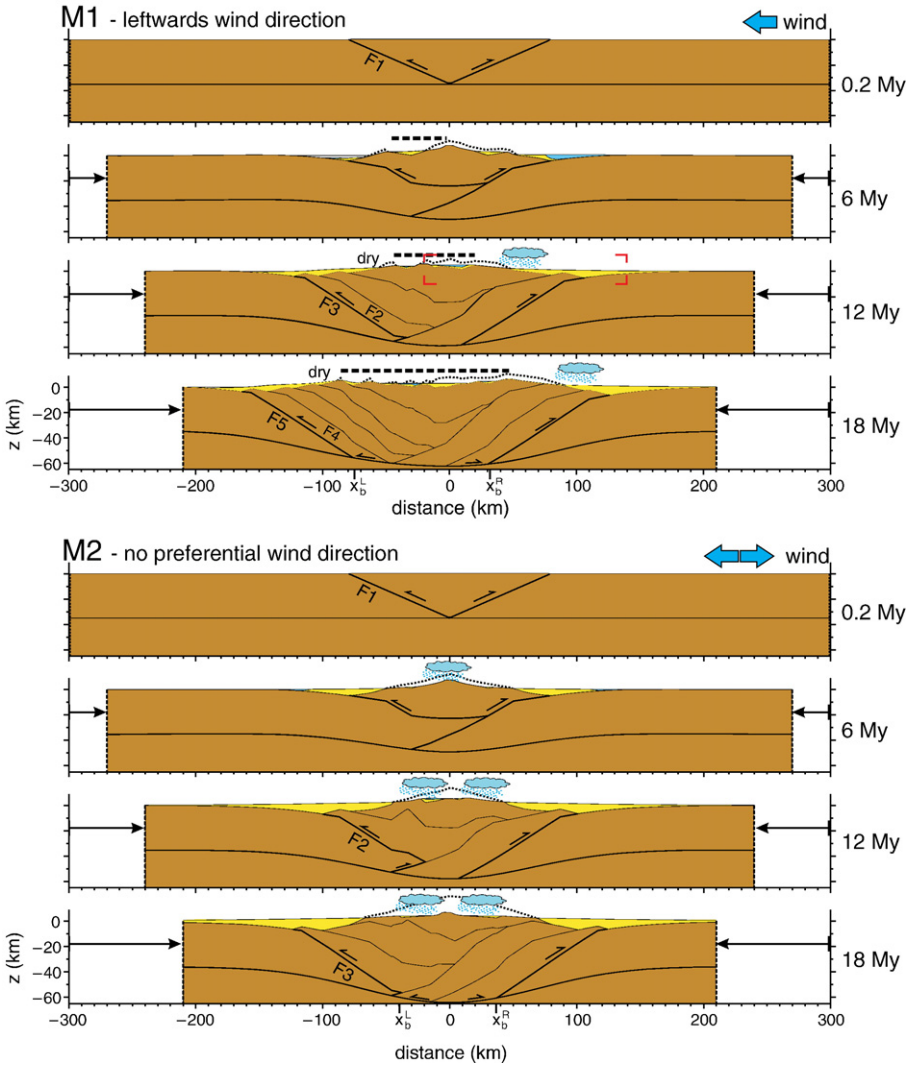

Fig. 3. Calculated evolution of models M1 and M2 showing the different location and timing of thrust faults due to different climatic parameters. All non-climatic parameters are identical for M1 and M2 as listed in Table 1. Eroded rock is indicated with dotted lines. Dashed horizontal lines in M1 indicate the location of endorheic basins. Clouds schematically indicate the concentration of precipitation (see Figs. 4 and 5). No vertical exaggeration. F1–F5 indicate the fault sequence in the left side of the orogens. Active faults are shown with bold lines. The reference frame is such that the orogenic wedge is fixed and both undeformed forelands move towards the center. The area framed in red in M1 ($t=12$ Myr) is zoomed in Fig. 4. Orographic rain shadow in the left side of M1 promotes the development of closed intraorogenic basins trapping most erosional products from the orogen, promoting in turn faster propagation of thrusting towards the external parts of the orogen. In contrast, the more humid weather and lack of rain shadow of M2 imply higher erosion rates that efficiently eliminate mass from the orogen and reduce pressure along active faults, prolonging their activity and slowing down the tectonic propagation into the foreland. Note the very symmetrical development of faults in M2, whereas the orographic effects in M1 induce more faults on the downwind (left) side.

Though this synthetic setting is not intended to reproduce data from a specific geological region, the Central Andes-Altiplano and the Western Alps are used here as sources of inspiration for most parameter values. Although these orogens have formed in very different tectonic settings (subcontinental subduction and continent–continent collision, respectively), the amount of continental shortening is comparable (Fig. 1). Differences between the Andes and the Alps are also important when looking at surface erosion and sediment transport (namely the >15 km of erosion in the axial Alps vs. the 3 km of sedimentation within the central Andes), and therefore they are adequate scenarios to validate the hypothesis of this work. The strategy is to find a synthetic tectonic setup that reproduces the main topographic, surface transport, and drainage features of both scenarios by modifying only climatic parameters. Because we are disregarding viscous flow in the lower crust and dumping all deformation as thrust-related, we define a laterally constant depth of the detachment level of $z_d = 35$ km, which will allow approximately matching the observed crustal thickening and topography. This value is in the top range of the 25–35 km deep detachment levels derived by McQuarrie and DeCelles [9] and other structural studies. The final internal geometry predicted by the model will have little in common with that inferred for the Andean Eastern Cordillera by McQuarrie and DeCelles [9], since only brittle deformation and one detachment level are considered here. In turn, the simplicity of the model will facilitate the interpretation of the results, which aim to be general rather than specific for the Andes.

Shortening rate is set constant through time to 10 km/Myr during an 18-Myr-long tectonic period. Given the model approaches described above, the implied 180 km of total shortening is accommodated 50% at each side of the orogen ($V = 5$ mm/yr). These parameters provide a compromise between the post-collisional tectonic shortening in the Alps and the continental syn-uplift shortening in the Andes, amounting to 140 km and more than 200 km respectively (Fig. 1).

Erosional parameters are taken from previous studies using the same surface processes formulation that was calibrated using long-term basin evolution data (e.g., [21]). A constant value of lithospheric equivalent elastic thickness is taken of $T_e = 14$ km, a relatively low value at global scale and a compromise between the highly varying values reported for the Central Andes and its foreland, ranging from 5 to 40 km [31], and for the Alpine Molasse Basin, ranging from 10 to 50 km [32,33].

Table 1
Input parameter values

	Parameter	M1	M2	M3	M4
Climate	RH, rel. humidity at boundary	0.9	$P = 400 + z_t^* 0.4$ mm/yr	$P = 800$	$P = 3000$
	u, mean wind velocity	1.4 m/s			
	Γ, atmospheric thermal gradient	6.5 °K/km			
	α, precipitation constant	3300 mm/yr			
	E_0, reference lake evaporation	1300 mm/yr	$E = 0$	$E = 1300$	$E = 800$
	β, evaporation constant	.5			
Lithology	l_f, distance of erodability				
	Bedrock	120 km			
	Sediment	30 km			
	l_s, dist. lake/sea sedimentation	15 km			
	K_f, river transport capacity	60 kg/m^3			
	K_d, diffusive transp. coeff.	0.1 m^2/yr			
Tectonics	V, half shortening rate	5 mm/yr			
	Shortening duration	18 Myr			
	S_0, cohesion	10^6 Pa			
	μ, μ_d friction coeffs.	0.50, 0.27			
	z_d, depth detachment level	35 km			
	$\Delta\sigma_{xx}$, horizontal stress	$5 \cdot 10^8$ Pa			
	T_e, elastic thickness (km)	14 km			
Computation	dx, grid resolution	0.5 km			
	dt_e, time step for erosion	0.001 Myr			
	dt_t, time step for tectonics	0.1 Myr			
	Total model length	720 km			

Models M1 to M4 differ only in climatic parameters. Models M2, M3, and M4 adopt pre-defined precipitation P and evaporation E values, and thus they do not use the orographic precipitation equations detailed in Appendix A.

Keeping these lithological and tectonic parameters unchanged, the model results shown hereafter differ only in the adopted climatic parameters (Table 1) and focus on the role of climate during the formation of high plateaus.

5. Results. Role of orographic precipitation and evaporation

In order to illustrate the controls exerted by climate on high plateau development and the potential formation of internally drained (intramountain) basins, two end-member model runs are shown. Runs M1 and M2 differ only in the imposed climatic parameters determining the balance between precipitation and evaporation. These are chosen so that the predicted lateral variations of precipitation are comparable to those observed across the Central Andes-Altiplano and the Western Alps. M1 incorporates orographically controlled precipitation as described in Appendix A. In contrast, run M2 has been designed to represent a situation where wind does not have a clear dominant direction over multiannual time scales and precipitation falls in comparable amounts along both sides of topography.

M1 assumes a mean wind velocity of 1.4 m/s towards the left and a relative humidity of the incoming air of 0.9. Other climatic parameters are listed in Table 1 (chosen to mimic the precipitation across the Central Andes, Fig. 1). The predicted evolution of model M1 is shown in Fig. 3. Two initial inverse faults accommodate

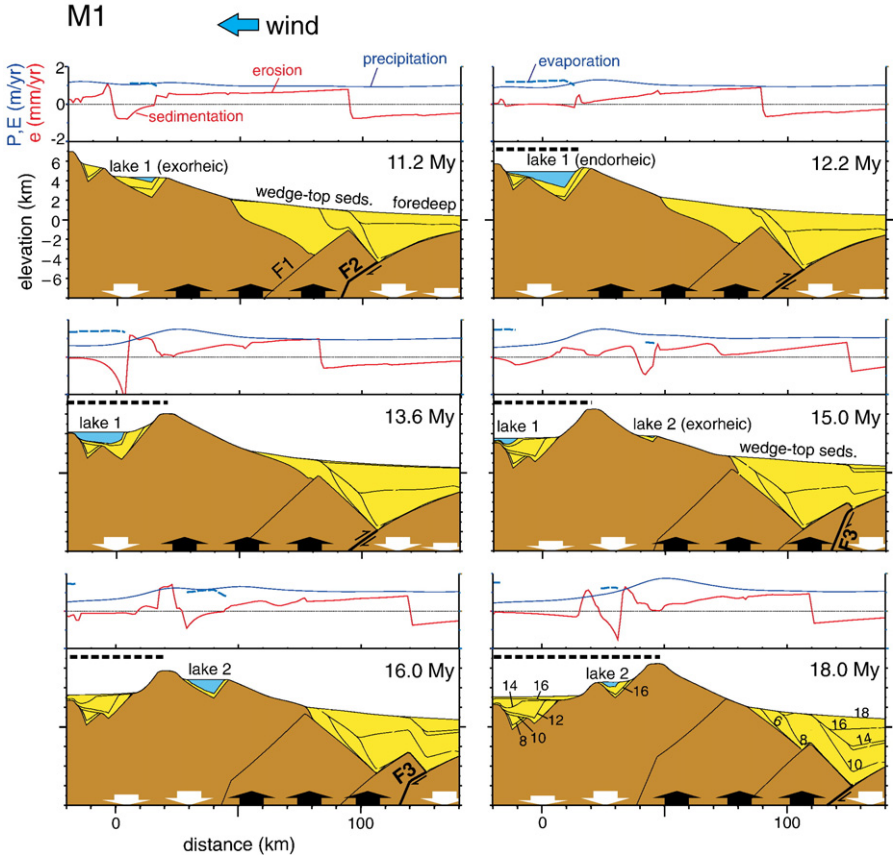

Fig. 4. Close-up view of the evolution of the right side of model M1 (location in Fig. 3, M1, $t=12$ Myr). Each time slice shows the distribution of precipitation (plain blue line) and evaporation (dashed blue line) in m/yr, rates of erosion (positive) and sedimentation (negative) in mm/yr are plot in red, and the resulting geometry of thrusts and sediment infill. Black lines in the sediments (in yellow) indicate sediment horizons and are labeled with ages in Myr in the last panel ($t=18$ Myr). Black and white vertical arrows indicate areas of tectonic uplift related to the active fault and areas of flexural isostatic subsidence. Vertical exaggeration 4:1. The sequence shows the incorporation to the endorheic area (marked with a horizontal dashed line) of two frontal lacustrine basins formed as a result of the activation of two thrusts (F2, F3) at $t=9.0$ and $t=14.8$ Myr. The calculated precipitation profiles reflect the orographic effects implemented through Eqs. (6)–(11), causing an orographic rain shadow downwind from the maximum topography, increasing evaporation E in that area, and favoring the formation and growth of an endorheic basin. Erosion is mostly restricted to the uplifting and elevated areas, whereas sedimentation takes place in lakes in the highlands and at marine deltas in the foreland basins, in both cases intercalated with fluvial aggradation.

all shortening, generating topography in competition with erosion and river incision, which remove rock from the surface. Note that in the model's reference frame both sides of the undeformed crust are moving towards the center, whereas the orogenic wedge is quiescent. As topography above the thrusts grows, so does the amount of frictional work required to continue deformation along them. At $t=7.2$ Myr, a new fault is formed on the

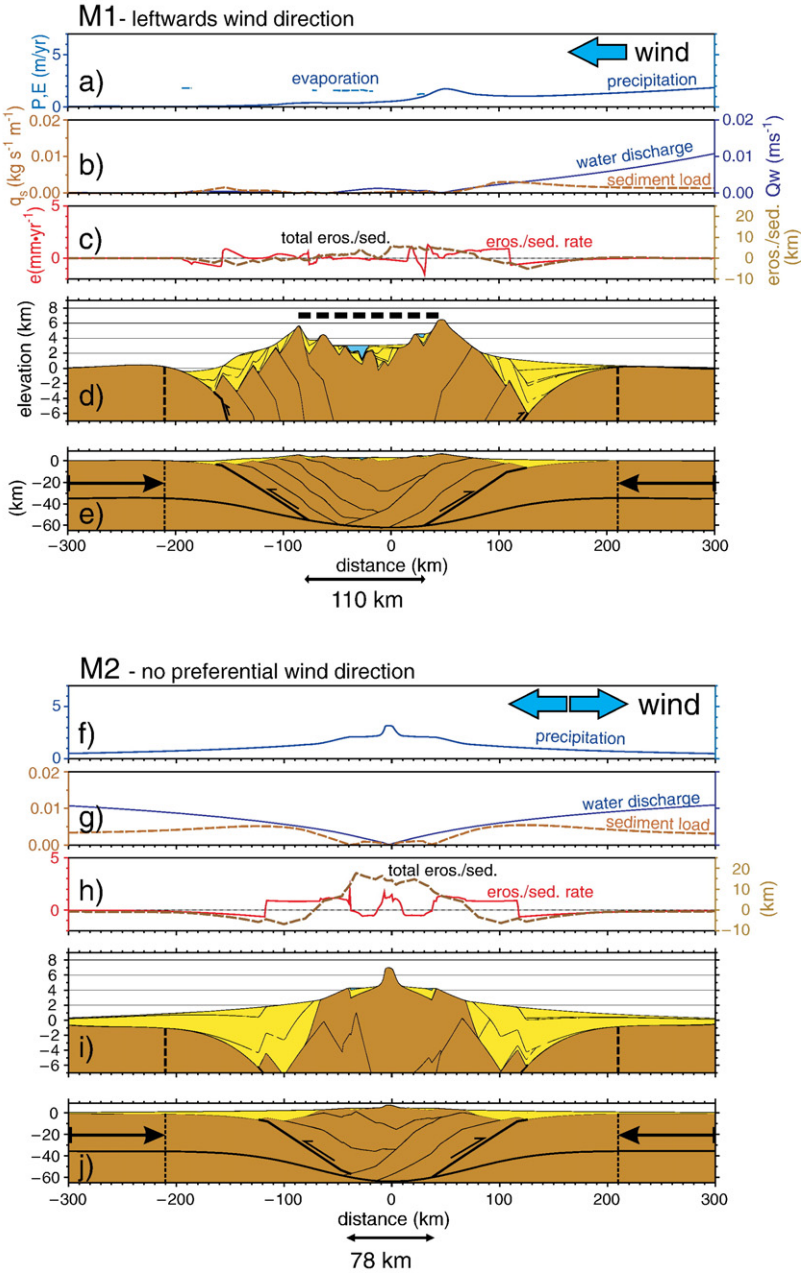

Fig. 5. Final stage of models M1 (left) and M2 (right) at $t=18$ Myr. (a, f) Precipitation (plain line) and evaporation (dashed line) as calculated by the climatic model. (b, g) Water discharge and sediment load. (c, h) Erosion/sedimentation rate at $t=18$ Myr (plain line) and total cumulative erosion/sedimentation (dashed line) expressed respectively in mm/yr and km of equivalent crustal density. Positive indicates erosion; negative for deposition. (d, i) Geometry of the upper kilometers of the model with a vertical exaggeration of 7:1 (yellow: sediment; blue: water). (e, j) True-scale display of the entire model. In M1, sediment accumulation has flattened and progressively increased the altitude of the endorheic basins, located at 3100–3600 m a.s.l. In contrast, fluvial incision in M2 is high enough to defeat tectonic uplift above thrusts, impeding drainage closure and facilitating removal of erosional products from the orogen. This in turn reduces the lateral growth of the orogen and impedes the formation of a high plateau.

left side which requires less work of activation than that necessary to continue deformation along the initial thrust (Fig. 3, M1, 12 Myr). The time when this happens is controlled by the amount of material removed by erosion from the orogen. The more efficient is erosion, the less rock remains above the fault and therefore less work is required to deform along that fault. For this reason, the very asymmetrical orographic precipitation across the orogen (Figs. 4 and 5) soon develops into an asymmetrical structural architecture, reflected in the larger amount of thrusts in the left side relative to the right side of the orogen (Fig. 3). Drier climate in the left side is also responsible for the important wedge-top sedimentation relative to the volume of foreland deposits, due to the reduced river transport capacity in that region. As topography grows, precipitation concentrates in the right-dipping slopes of the orogen, as dictated by Eqs. (6)–(8) (see Appendix A). Because precipitation and erosion are focused on the right side of the orogen (Fig. 4)), the orogen widens slower on that side. A second consequence of the competition between surface processes and faulting is the formation of lakes behind each fault (Fig. 4 and Fig. 2). Lakes form unless imposed shortening rates are one order of magnitude lower than the 5 mm/yr adopted in this paper. The widening of the orogen implies an increase of the surface available for lake evaporation. If evaporation and shortening rates are high enough, and the orographic rain shadow reduces sufficiently precipitation in the center of the orogen, the widening of the orogen can eventually induce (as in M1) the formation of an endorheic basin where all collected sediment and water are locally deposited and evaporated, respectively. Every new thrust forming in the external parts of the orogen generates a lacustrine basin that is eventually incorporated to the endorheic basin (Fig. 4). Note that the more rain falling in the upwind side of the orogen, the drier the air becomes in the central and downwind areas, promoting higher evaporation rates. Closed drainage (or endorheism) implies that, although some precipitation occurs in the highlands, its effect in terms of mass removal from the orogen is null.

With the disruption of the early drainage flowing from the orogen axis toward the forelands (Fig. 4, $t=11.2$ and 12.2 Myr), lacustrine basins formed by tectonic uplift become endorheic sediment traps as evaporation equals collected precipitation. Such sediment traps progressively fill with sediments developing into low relief areas at high altitudes, i.e., high plateaus. Sedimentation in this intramountain basin starts when it is no longer affected by thrust uplift. Wedge-top sediments, in turn, are affected by uplift, which explains the important altitude they reach in the dry side of the orogen (Fig. 5d, M1), where the incision of rivers is limited.

To simulate a climate with no preferential wind direction such as in the Alps, producing an approximately symmetrical precipitation pattern, model M2 assumes a precipitation distribution dependent only on topography and a constant evaporation along the entire section. In particular, $P=400+z_t[\mathrm{m}]\cdot 0.4$ mm/yr, and $E=0$ mm/yr are adopted, resulting in the precipitation pattern displayed in Fig. 5f.

Fig. 3 shows the evolution of model M2. Although lakes also form in model M2 behind active faults, river incision is efficient enough to overcome tectonic uplift, and soon after a fault becomes inactive the associated lake is filled by sediments and/or reintegrated to the river profile by outlet erosion (see details in [22]). The highlands receive here the highest amount of precipitation, impeding closure of potential lakes. As a consequence, intramountain sedimentary basins in this model are much smaller and more ephemeral than those in M1 and no long-living basins form that can develop into a high plateau. This results not only in higher erosion rates but also in a more efficient evacuation of the erosional products towards the foreland basins and therefore a significant reduction of orogen width relative to model M1. Note that the resulting orogenic structure is approximately symmetric (similar distribution of thrusts at each side of the orogen) in M2 because both climate and tectonics have symmetrical predefined conditions.

Whereas in model M2 up to 16.5 km of basement rock is eroded (Fig. 5h) and transported to the foreland basins and beyond (Fig. 5g and i), in M1 most of the eroded rock is trapped within the orogen and at orogenic scale the effective mass removal is small (Fig. 5c). At $t=6$ Myr (Figs. 3 and 6), for example, the average precipitation at the orogen is 85% larger in M2 than in M1, implying a mean erosion rate 20% higher in M2 and a lesser lithostatic pressure at the detachment level in this model (locally up to 15%); this is ultimately responsible for the earlier activation of the second pair of faults in M1 relative to M2 (Fig. 3; see also Appendix A). Shortening is accommodated along fewer faults in M2, resulting in a narrower orogen relative to M1. Consequently, tectonic uplift in M2 is concentrated along a shorter distance along the section (from $x=-120$ to $x=+120$ km). This explains the apparent paradox of M2 simultaneously undergoing higher erosion rates and higher peak altitudes.

Although the emphasis of this modeling is providing an easy comparison between results from M1 and M2,

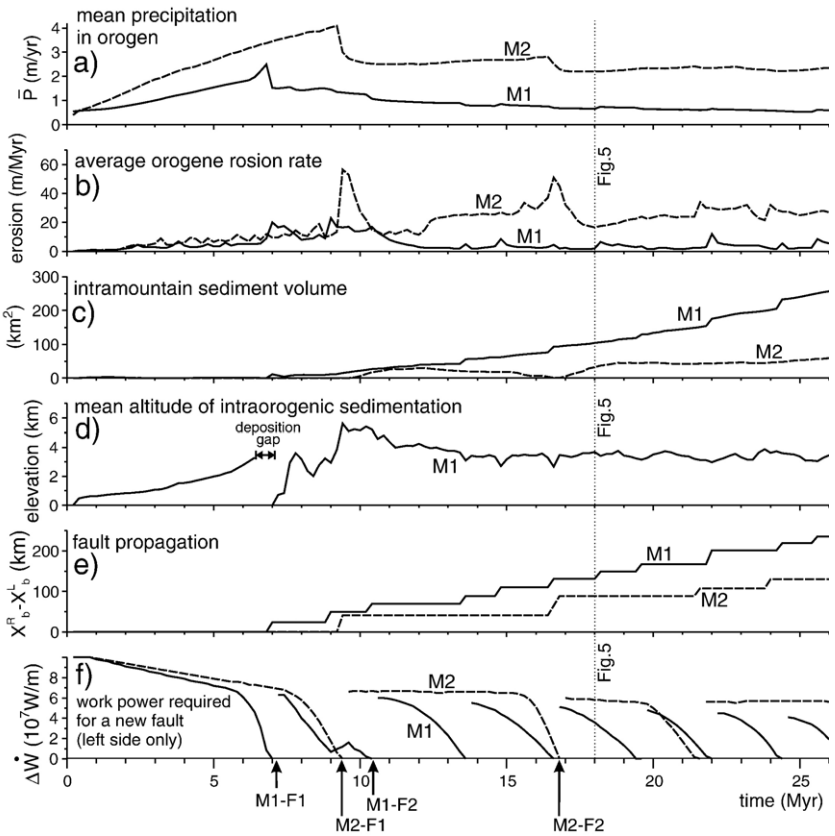

Fig. 6. Evolution of parameters in M1 (plane lines) and M2 (dashed lines): (a) mean precipitation in the orogen. (b) Average erosion/deposition rate in the orogen. (c) Volume of intramountain sediment. (d) Average altitude of deposition in the intraorogenic basin. (e) Distance from x_b^L to x_b^R (i.e., width of the non-uplifting intraorogenic area). (f) Tectonic power required to generate a new fault (if zero then a new fault is generated; only displayed for the left side). Differences in erosion between models M1 and M2 are responsible for the different work required to maintain the imposed shortening rate and for the different timing of the faults.

rather than reproducing a precise geometry and tectonic evolution of specific geological scenarios, several features of M1 and M2 are comparable to the aspects of the two end-member examples mentioned in Introduction. The last stage of M1 (Fig. 5) predicts topographic features (Fig. 5d) similar to the present-day Andes, such as a nearly 300 km-wide orogen with maximum altitudes above 6000 m at two cordilleras surrounding a central internally drained depression: a high plateau between 3000 and 4000 m altitude containing central endorheic lakes of variable depth. In turn, M2 predicts topographic features closer to the present-day Western Alps: Fig. 5f–j shows a 240 km-wide orogen with maximum altitudes in the central area and two flanking, overfilled foreland basins. Also the predicted Moho depth and the amount of erosion are comparable to the observed values (Fig. 1), despite the fact that the assumed shortening rate is a compromise between Andean and Alpine values. For the same reason, the amount of erosion from the central area overestimates by ~10% the exhumation derived from thermochronological studies of the Alps (e.g., [34]).

The evolution of some properties of models M1 and M2 is compared in Fig. 6. The higher precipitation falling on the highlands in M2 induces the evacuation of important amounts of eroded material from the orogen, whereas in M1 the small amount of sediment eroded is mostly trapped within the orogen and the material leaving the orogen remains close to zero (Fig. 6b and c). As a result, the work consumed at faults is larger in M1 and therefore more thrusts (and more distal) develop in that model, leading to a wider orogen. High plateau surface uplift in M1 is caused by the combined effects of thrusting (tectonic uplift), flexural rebound due to erosion of the orogen once thrusting propagates forward into the foreland, and sediment accumulation. Interestingly, these mechanisms contribute to increase the altitude of deposition in few million years (between $t=7$

and 10 Myr; Fig 6d), similar to what oxygen isotopes in carbonates, edaphological, paleosol, and palustrine carbonate data suggest for the Altiplano [10].

Imposing laterally constant values of P and E provides a simple way to display the effects of these parameters on surface mass transport and the final orogen structure. Runs M3 and M4 are identical to M1 except that they assume a constant evaporation rate of $E=1300$ and 800 mm/yr respectively and a precipitation $P=800$ and 3000 mm/yr respectively. Both models are shown in Fig. 7. Smaller precipitation rates and higher evaporation in M3 relative to M4 result in a reduction of water discharge at $t=18$ Myr. This induces smaller erosion of the thrusting units in M3 and an increase of

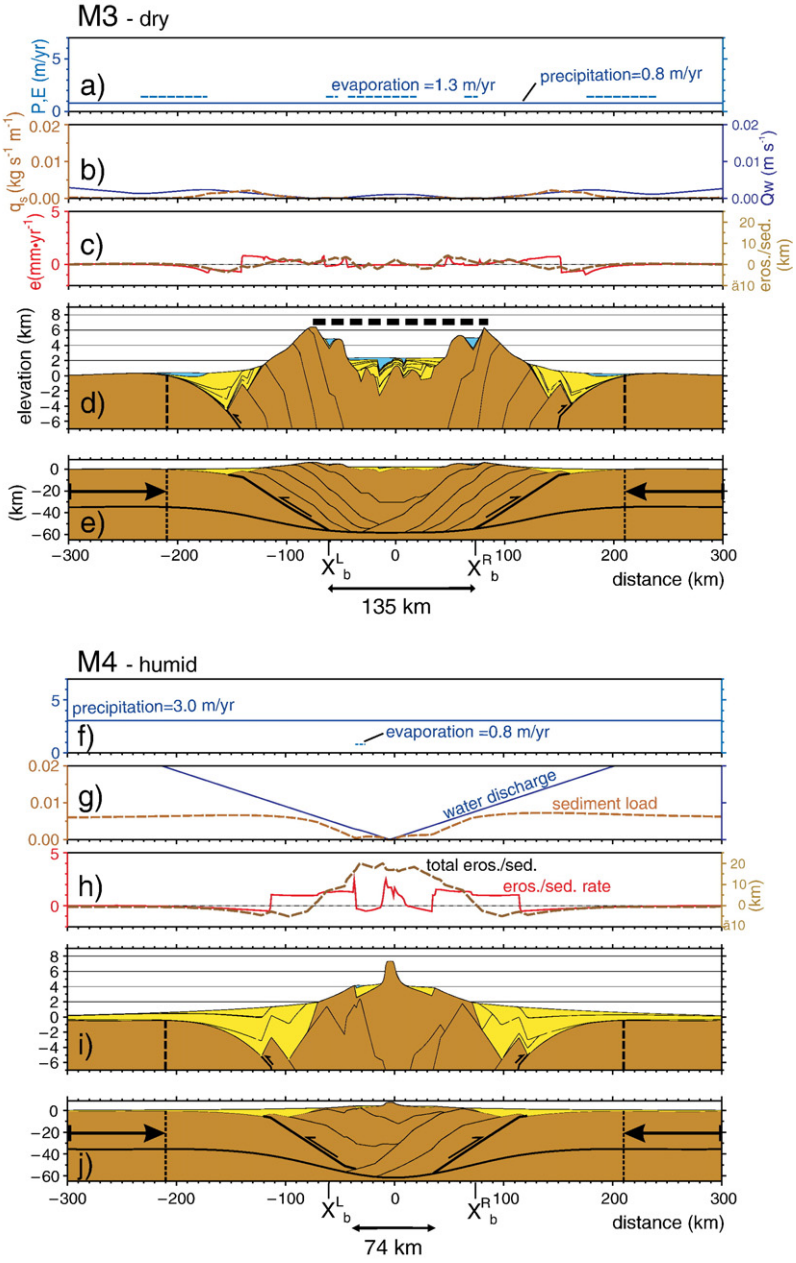

Fig. 7. Final stage of M3 (dry) and M4 (humid) at $t=18$ Myr. Input parameters are identical to M1 and M2 (Fig. 5)), except for precipitation, which is laterally constant for these models ($P=500$ and 3000 mm/yr respectively), and evaporation ($E=1400$ and 800 mm/yr). Legend as in Fig. 5. The symmetrical precipitation pattern adopted for M3 results in a more symmetrical orogen geometry relative to M1 (Fig. 5), in terms of fault and sediment distribution.

lithostatic pressure along faults, resulting in earlier fault deactivation and further propagation of deformation.

The simplified setting M4 is used to parameterize the effect of precipitation (Fig. 8). The volume of intramountain sediments, the altitude of deposition, and the intramountain width (all at $t=18$ Myr) are plotted as a function of P, keeping E constant. Whereas the altitude reached by the intramountain sediment infill is relatively independent of P, the orogen half-width (or fault propagation, here approximated as the distance between x^{L}_{b} and x^{R}_{b}, see Figs. 2 and 7) and the amount of sediment trapped in it both decrease for increasing precipitation values. Beyond a critical value of $P_c=3500$ mm/yr erosion is so rapid that no intramountain basin is formed. For values higher than ~1000 mm/yr the high plateau is not formed (the relief is not reduced significantly within the orogen and drainage does not become endorheic). Although these absolute values are subject to the limitations of the model (e.g., the 2D approach), the trends shown in Fig. 8 show that, within the approaches of the model, climate is capable of determining on its own whether a high plateau is formed or not.

6. Interpretation and discussion in the light of recent climate data from the Andean high plateau

High plateaus have been generally interpreted as the result of viscous flow at lower crustal levels, strain partitioning related to inherited tectonic structures, thermal perturbations in the lithosphere, and other tectonic processes (e.g., [1]; [11]; [35]). The present study does not address the influence of these processes, but focuses on quantifying the additional role played by climate-controlled surface processes. The results suggest that dry climate prior and coeval to uplift might contribute to strain partitioning in the Andes and to the formation of the Altiplano between the Eastern and Western Cordilleras. Note that the mechanism proposed here is completely independent of that proposed by Lamb and Davis [36]. Whereas these authors suggest that climate has controlled sediment delivery to the trench and friction along the subduction plane, thus influencing its tectonic coupling, here I propose that intramountain sediment trapping imposed by drainage closure contributes to propagate tectonism towards the external parts of the orogen and to develop the high plateau. The way surface mass transport undertakes this role is in essence similar to how sedimentation in subduction wedges seems to reduce deformation within the accretionary wedge itself [37]: ultimately, erosion and sedimentation modify the lithostatic pressure distribution, the dynamic equilibrium between orogenic forces, and the lateral vs. horizontal orogenic growth as proposed by Molnar and Lyon-Caen [38].

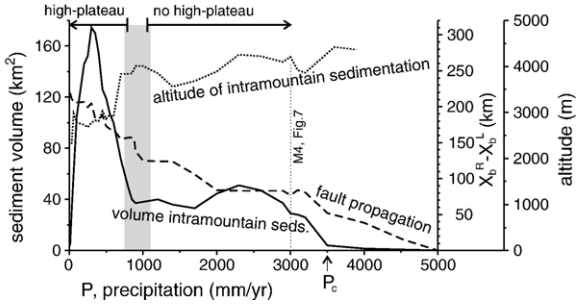

Fig. 8. Effect of precipitation P on the high plateau resulting at $t=18$ Myr, all other parameters remaining as in M4 (Table 1). Whereas the average altitude of intramountain sedimentation (dotted line) is relatively insensitive to P but largely controlled by tectonic parameters, the width of the non-uplifting intramountain area (dashed line, representing the distance between x^{L}_{b} and x^{R}_{b}, see Fig. 7) and the volume of the intramountain basins (plain line) decrease significantly with P. Virtually no intramountain basin is preserved for $P>3500$ mm/yr and a high plateau develops only for precipitation values lower than evaporation, i.e., $P<800$ mm/yr.

According to the results of the present study, dry conditions (low P, high E) during the early stages of uplift cancel sediment evacuation from the center of the incipient orogen by generating internally drained intramountain basins (Fig. 9). The results from models M1 and M2 are not just suggesting that this "little erosion implies higher mountains" (in fact the humid model ends up with a higher maximum topography than the dry one) but something subtler: that the presence of climatic-controlled endorheism can modify the tectonic deformation in orogens contributing to strain partitioning and promoting the formation of high plateaus. As topography grows tectonically, orographic effects on precipitation block the inflow of humid air into the intramountain area and reinforce endorheism. Such sediment trapping increases pressure at crustal levels below the orogen. The difference between >15 km of erosional mass removal from the axial Alps (Fig. 1) and the >3 km of syn-orogenic deposition within the Andean Altiplano implies that pressure at the detachment level is >60% higher in the Andes. This pressure increase promotes fault propagation towards the external parts of the orogen, reinforcing the orographic effects on precipitation and the climatic isolation of the intramountain basin. From this point of view, endorheism is a mechanism promoting intraplate deformation, and endorheic conditions in intracontinental areas such as central Asia might be seen as partially responsible for

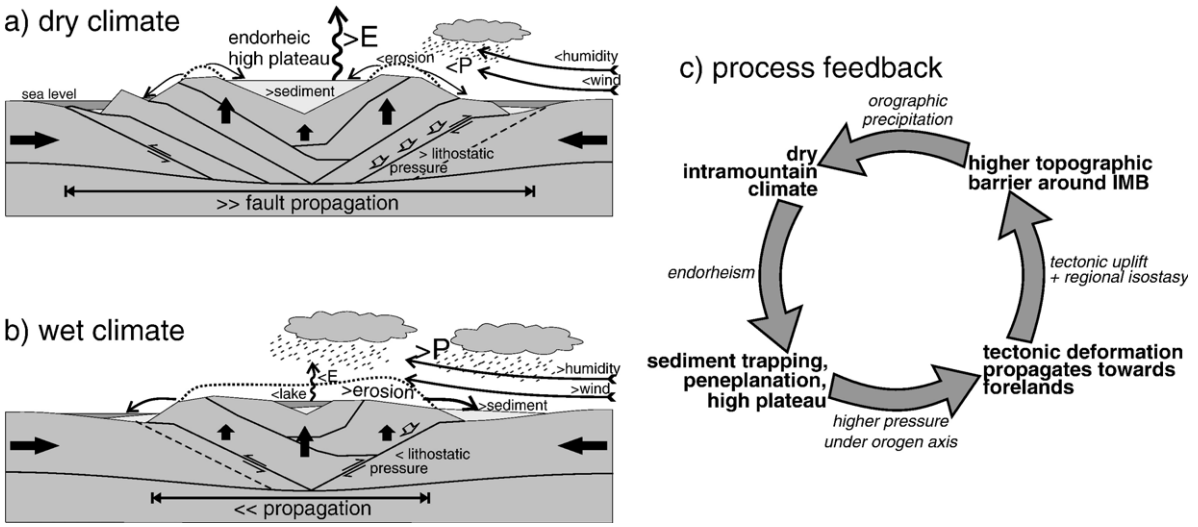

Fig. 9. Schematic cartoon summarizing the process feedback contributing to the formation of internally drained basins and high plateaus in orogens. (a) Low precipitation and high evaporation favor the closure of intramountain basins, dramatically reducing evacuation of sediments from the orogen. Such sediment trapping increases the pressure along faults in the orogen axis, enhancing propagation of deformation into the foreland and reinforcing the climatic isolation of the highlands. (b) In contrast, humid weather inhibits the formation of endorheic basins and promotes evacuation towards the forelands, reducing pressure along faults and keeping them active for a longer period of time. Shortening is differently accommodated in terms of uplift (black arrows). (c) depicts the proposed processes feedback leading to high plateau formation. In (a) and (b), '<' and '>' indicate smaller and higher parameter values relative to each other. IMB stands for intramountain basin.

the propagation of deformation into continents, rather than just as a result of it.

Taking into account the model limitations described earlier (namely the 2D approach and the simplicity of the tectonic model), the results indicate that dry climate contributes to the development of high plateaus in the following steps (Fig. 9c): (1) tectonic shortening propagates towards the foreland favored by low erosion rates related to dry climate; (2) most precipitation concentrates on the fore-front topography, whereas the hinterland area downwind from the frontal thrusts becomes even drier and drained by rivers with reduced incision power; (3) tectonic uplift eventually defeats the river channel and closes the intramountain basin, which becomes internally drained due to the prevailing low precipitation and high evaporation [20,21]; (4) ongoing sedimentation in the endorheic basin ensures increase in elevation and peneplanation of the basin; (5) reduced evacuation of erosional products along the axis of the orogen increases lithostatic pressure at crustal levels, inhibiting deformation in that area and promoting thrust propagation towards the external parts of the orogen, which are progressively incorporated to the endorheic basin. This feedback effect implies that the presence of dry climate during the early stages of orogenesis promotes future lateral growth of the orogen and the incorporation to the high plateau of the basins originated in the external parts.

In regard to the formation of the Andean Altiplano, it has long been assumed that dry climate began in the Chilean–Peruvian coastal desert as a result of uplift and orographic isolation. However, recent works based on paleomagnetic, sedimentological and cosmogenic data suggest that dry climate actually predated the main uplift phase [39,40]. Paleosols of the Calama Basin, about 20 Ma in age and consisting of vertisols containing soil carbonate, suggest precipitations lower than 700 mm/yr at that time [41]. The present-day location of the Atacama basin within the dry subtropical belt is the principal cause for aridity, and this situation is likely to have prevailed since late Jurassic, enhanced by the continentality effect exerted by the Gondwanan land-mass and by the presence of an offshore, cold, upwelling current (since at least the early Cenozoic and possibly earlier), resulting in conditions promoting climatic stability and desert development [40].

As for the eastern flank of the southern Central Andes, at least transient internally drained conditions existed in the Puna region from ca. 29 to 24 Ma [42,43] as reflected by thick evaporite units in the late Miocene in the Salar de Antofalla. Eocene evaporites and evaporitic paleosols are also reported in the Bolivian

Eastern Cordillera [44]. These deposits testify the beginning of the process of disruption of the regional fluvial system that may have led to internal drainage. Recent thermochronological and sedimentological data [43] suggest that deformation and uplift of the southern Puna plateau were active already in Oligocene time and contributed to the fragmentation and drainage reorganization of an earlier semicontinuous foreland basin. But this event occurred in an already arid environment that provided the ideal conditions for the establishment of the subsequent internal drainage that was in place by middle Miocene time.

In summary, there are today solid evidences of arid conditions predating uplift in the Central Andes (and later enhanced by it). The modeling presented here suggests that such dry climate did in fact contribute to the formation of the Altiplano by helping to partition tectonic deformation, rather than being just a passive result of uplift. In order to determine the importance of this mechanism relative to inherited structures and tectonic controls, future work should address this process interaction via more sophisticated numerical models that account for the complex dynamics of the lithosphere under compression and/or the marked 3D character of surface mass transport.

Acknowledgments

I am indebted to Muriel Gerbault and Andrés Tassara for their encouragement and for the criticisms and suggestions on the mechanical approaches and the tectonic evolution of the Andes. The paper has benefited from detailed and thoughtful reviews by Peter G. DeCelles and an anonymous reviewer. Discussions with David R. Cook have been helpful in fine tuning the climatic model. Dennis Brown, Andrés Pérez-Estaún, Manel Fernàndez, and Joaquina Álvarez-Marrón are acknowledged for their comments on the manuscript. Funded by the *Ramón y Cajal* program of the Spanish *Ministerio de Educación y Ciencia* (CGL2006-05493; CSD2006-00041).

Appendix A. Formulation

The processes implemented can be divided in four groups: brittle tectonic deformation of the crust; atmospheric precipitation, evaporation, and balance between atmospheric water and fluvial/lacustrine water flow; surface processes of erosion, river transport, and deposition; and flexural isostatic response of the lithosphere. In this section the approaches adopted to simulate these processes are explained in detail.

A.1. Tectonic deformation

To simulate tectonic deformation in cross-section we follow the simplest approach capable to reproduce the dynamics of fault propagation towards the external parts of the orogen. Note that the aim here is not to reproduce in detail specific fault systems but to study the mutual effects between surface processes and tectonic deformation through simple, synthetic scenarios. This model is modified after a minimal work criterion of brittle deformation by Masek and Duncan [45], incorporating approaches to the work consumed against friction and gravity during tectonic shortening.

The rate of dissipated frictional work $\dot{W}_f$ (measured in power units) along a fault is approached as:

$$\dot{W}_f = V' \int \tau \mathrm{d}l \tag{1}$$

where V' is the shear velocity along the fault, τ is the shear stress along the fault and l is the distance along the fault. Note that this power is expressed in watts per unit length perpendicular to the modeling plane [W m^{-1}]. The shear stress at the fault is approached via Anderson's theory as the component of normal stress (perpendicular to the fault plane) multiplied by a slip friction coefficient μ [45]:

$$\tau = S_0 + \mu\left(\rho_c \cdot g \cdot (z_t - z_f) + \frac{\Delta\sigma_{xx}}{2}(1-\cos 2\theta)\right) \tag{2}$$

Where S_0 is the cohesion, assumed to equal 10^6 Pa at new forming faults and 0 at active faults to account for the preference of deformation along existing faults relative to new ones. θ is the dip angle of the fault, ρ_c is the density of the crust, g the acceleration of gravity, z_t (x) the topographic altitude, and $z_f(x)$ the altitude of the fault. $\rho_c g(z_t - z_f)$ is therefore the lithostatic pressure at the fault, whereas $\Delta\sigma_{xx}$ represents the horizontal tectonic stress. θ, μ, z_f, and z_t vary along the modeling profile, whereas $\Delta\sigma_{xx}$ is assumed constant. In first approach, the friction coefficient μ determines the faulting angle θ through this relationship (e.g., [46]):

$$\mu = \frac{1}{\tan 2\theta} \tag{3}$$

θ usually ranges between 25 and 40° as inferred from compressional deformation structures in the field and in analogue experiments, implying μ values ranging between 0.2 and 0.8. Hereafter it will be assumed in this work that thrusts follow an initially horizontal detachment (at $z_d = 35$ km depth in our reference model)

and reach the surface following a linear path at $x>x^{R}_{b}$ ($x<x^{L}_{b}$ in the left side of the orogen). Taking these assumptions into account, the expression for the power dissipation along the active fault is

$$\dot{W}_{\mathrm{f}} = V\int_{x<x_b}[S_0+\mu_{\mathrm{d}}\rho_{\mathrm{c}}g(z_{\mathrm{t}}-z_{\mathrm{d}})]\mathrm{d}x + \frac{V}{\cos^2\theta}\int_{x\geq x_b}\left[S_0+\mu\left(\rho_{\mathrm{c}}g(z_{\mathrm{t}}-z_{\mathrm{f}})+\frac{\Delta\sigma_{xx}}{2}(1-\cos 2\theta)\right)\right]\mathrm{d}x \tag{4}$$

where V is the shortening velocity, x is the horizontal coordinate, z_{d} is the depth of the detachment level, the first term of the right side is the frictional work along the detachment, and the second term is the work along the ramp. Friction coefficients of $\mu_{\mathrm{d}}=0.1$ along the detachment level and $\mu=0.5$ elsewhere are adopted for this paper, implying that thrusts reach the surface from the detachment level following an angle $\theta=30°$ (Eq. (3)).

As for the power consumed against gravity (i.e., by increasing the potential energy of the thrusting sheet), it can be calculated as the product of the vertical velocity along the fault multiplied by the rock weight above the fault:

$$\dot{W}_{\mathrm{g}} = \int\left(V\tan\theta-\frac{\mathrm{d}w}{\mathrm{d}t}\right)\rho_{\mathrm{c}}g(z_{\mathrm{t}}-z_{\mathrm{f}})\mathrm{d}x \tag{5}$$

where $\mathrm{d}w/\mathrm{d}t$ is the derivative of the flexural deflection w (detailed later in this section). Adding $\dot{W}_f$ and $\dot{W}_g$ and disregarding the work dissipated by the internal deformation of the thrust sheet provide the total work consumed by a given tectonic shortening rate V. As topography grows, pressure along the active fault increases Eq. (2) and so does the frictional work necessary to maintain the shortening velocity V. The work consumed against gravity also increases as topography grows above the fault ramp. Hence, because of the low friction along the detachment level, the total work can eventually become larger than the work required along a new fault with an x'_{b} position further into the undeformed foreland (Fig. 2). This triggers in our model the activation of a new thrust that will accommodate all shortening taking place in its side of the orogen. The tectonic units defined by faults move towards the undeformed foreland according to a vertical shear approach (i.e., preserving their vertical thickness), which allows for an easy implementation of mass conservation. Faults cut also through the sediment, which is tectonically transported, also preserving its mass.

Such model does not account for a diversity of deformation processes known to take place during orogenesis. It is, for example, unlikely that brittle deformation is a valid approach down to more than 35 km as it will be assumed later on. More important, the geometry imposed to the faults and the inability to accommodate shortening along more than two active faults are very restrictive. Rather than complicating the experiments with a fully thermodynamic elastic–visco–plastic approach that would dramatically increase the number of unknown parameters, I opt for assimilating all deformation as brittle, assuming that whatever other mechanisms are present they would respond in a similar manner to the tested changes in surface transport. The model must be seen therefore as the simplest way to calibrate the first order influence of surface transport on the propagation of tectonic deformation (similar to [45]).

A.2. Climatic and hydrological processes

Surface flow of precipitation waters is the main process performing surface sediment transport. The level of water saturation of the air determines the water exchange between the air and the surface of the earth (evaporation/precipitation). The maximum water content in an air column $A_{\max}$ (measured in m) can be derived from the Clausius–Clapeyron equation (e.g., [47]):

$$A_{\max}(x) = \int_{z_{\mathrm{t}}}^{\infty}\rho_{\mathrm{v}}(z)\mathrm{d}z = \int_{z_{\mathrm{t}}}^{\infty}\frac{e_{\mathrm{s}}(z)}{R_{\mathrm{v}}T(z)}\mathrm{d}z = \int_{z_{\mathrm{t}}}^{\infty}\frac{e_{s0}}{R_{\mathrm{v}}T(z)}\exp\left(\frac{L}{R_{\mathrm{v}}}\left(\frac{1}{T_0}-\frac{1}{T(z)}\right)\mathrm{d}z\right) \tag{6}$$

where z_{t} is the ground elevation, ρ_{v} is the vapor density, e_{s} is the saturation vapor pressure at a given temperature T, $R_{\mathrm{v}}=461.5$ J kg^{-1} K^{-1} is the vapor gas constant, and $e_{s0}=611$ Pa is the saturation vapor pressure at $T_0=273$ K. Air temperature varies with height above the ground ($z-z_{\mathrm{t}}$) as

$$T(z) = T_{\mathrm{zt}}-\Gamma\cdot(z(x)-z_{\mathrm{t}}(x));\ T_{\mathrm{zt}} = T_{\mathrm{sl}}-.004\cdot z_{\mathrm{t}}(x) \tag{7}$$

where T_{zt} is the ground temperature (at $z=z_{\mathrm{t}}$), T_{sl} is the temperature at sea level, in K, and $\Gamma=0.0065$ K/m.

The actual water content in the air column A is the result of the incoming humid air, the evaporation

supplied from the solid Earth surface and the precipitation. Applying vapor mass conservation, the spatial derivative of A is

$$\frac{\mathrm{d}A(x)}{\mathrm{d}x} = -\frac{P(x)}{u} + \frac{E(x)}{u} \tag{8}$$

where dx is a distance increment in the direction of the wind, P is the precipitation, E the evaporation, and u is the mean horizontal wind speed. Such approach captures the vapor mass balance between the incoming wind and the evaporation/precipitation exchange with the ground, which has been neglected in previous models of tectonics–climate interaction but is of capital importance in this paper because humid air is expected to cross a series of topographic highs and lows containing lakes that reload the air with moisture.

Vertical movements of the air induce an approach or retreat of A from the saturation value $A_{\max}$. Atmospheric precipitation results mostly from water condensation by quasi-adiabatic air decompression and cooling during uplift. Such uplift occurs in two main ways: by overcoming an orographic obstacle, and by local turbulent flows. These two mechanisms are captured in the following expression:

$$P'(x) = \alpha \frac{A(x)}{A_{\max}(x)} \tag{9}$$

where P' is the precipitation produced by the air column above any given location x, and α is a constant controlling the precipitation occurring due to turbulent air flow even when saturation is not reached. Processes such as air uplift or humidity reload over a lake may result in $A > A_{\max}$ (saturation) and then $A - A_{\max}$ is instantaneously dumped as precipitation P'. Note that the orographic effect on precipitation is contained in $A_{\max}$, since this strongly decreases with altitude. The effect of continentality is captured because A is reduced by precipitation as air moves inland. The adopted boundary condition is $A = A_{\max} \cdot \mathrm{RH}$ (RH is the relative humidity of the incoming wind, see Table 1) and therefore precipitation in the boundary is $\alpha \cdot \mathrm{RH}$.

Following Roe et al., 2003 [60], I implement lateral smoothing of this orographic precipitation, related to non-instantaneous water condensation, local turbulence, and deviations from the mean wind velocity adopted values, so that the precipitation P falling at x is:

$$P(x) = \frac{2}{\Delta x\sqrt{\pi}} \int_{-\infty}^{\infty} P'(x') \cdot \mathbf{e}^{-\frac{x-x'}{\Delta x}} \mathrm{d}x' \tag{10}$$

where $\Delta x = 10$ km is the smoothing length. Precipitated water P flows along the surface in the model following the steepest slope.

Previous computer models of long-term surface transport did not account for evaporation. Whereas evapotranspiration along the river network can be easily accounted for as a reduction in local runoff or precipitation, evaporation at the surface of lakes must be explicitly incorporated if closed drainage basins are to be generated. Here an approximation is adopted according to which evaporation increases linearly with wind speed (similarly to [47]) and with $A_{\max} - A$:

$$E(x) = E_0(1 + \beta u)\frac{A_{\max} - A}{A_{\max}} \tag{11}$$

where E_0 is a reference evaporation rate for a hypothetical dry and static air (if incoming air humidity and wind speed were zero), β is a constant determining the dependency with wind velocity, and u is the absolute value of mean wind velocity.

In absence of significant underground flow, the level of a closed lake is determined by the water balance between precipitation and evaporation, which in a steady state situation can be written as

$$P \cdot W_{\mathrm{cb}} = E \cdot W_{\mathrm{cl}} \tag{12}$$

where P is the mean precipitation rate in the lake's hydrographic basin of width W_{cb}; E is the evaporation at the lake's surface; and W_{cl} is the width of the closed lake. Note that in this paper P is referred to as precipitation but in fact it represents only to the component collected as surface runoff, since infiltration and non-lacustrine evapotranspiration are not explicitly taken into account.

If the lake water level reaches the outlet, drainage becomes open and outlet incision leads to the integration of the lake into the drainage network (drainage capture). During capture, the output discharge of the lake is $P \cdot W_{\mathrm{b}} - E \cdot W_{\mathrm{l}}$. The width W_{l} of the lake is related to its water level z_{l} by the hypsometric curve. Within the adopted 1D approach, this hypsometric curve is expressed in terms of lake width W_{l} below any altitude z, and coincides with the lake bathymetric profile. By definition, $W_{\mathrm{l}}(z_{\min}) = 0$ and $W_{\mathrm{l}}(z_{\max}) = W_{\mathrm{cl}}$, where $z_{\min}$ corresponds to the minimum elevation of the lake floor, and $z_{\max}$ corresponds to the outlet level at the time of opening.

In an open drainage situation, the water excess (i.e., the water not being evaporated) leaves the lake along the outlet river

$$Q_{\mathrm{w}}(x) = E \cdot (1 - W_{\mathrm{l}}(z_{\mathrm{l}})) + K_{\mathrm{H}} x^h \tag{13}$$

where x is measured from the outlet in opposite direction to the lake (i.e., towards the escarpment) and the second term corresponds to Hack's Law of river water discharge. For simplicity we use $h=1$, so that K_H equals precipitation $P(x)$.

A.3. Erosion, sedimentation and surface sediment transport

Studies of river incision and sediment transport have provided quantitative models of landscape evolution driven by surface water flow (e.g., [48]). These models have been useful to quantitatively understand the processes leading to the tectonic defeat of antecedent rivers [49,50] and the formation of intramountain basins [20]. According to these results, the main factors controlling river diversion or defeat are the mean precipitation in the catchment, the rate of tectonic uplift across the river path, and the rock strength of the uplifting area. However, these models do not address the formation of lacustrine endorheic system upstream from the tectonic barrier and the water balance between collected runoff and evaporation at the lake's surface. This is of key relevance here because by definition the transition from an intramountain basin to an internally drained high plateau requires the evaporation at the basin to compensate the collected water runoff.

Erosion is modeled via a combination of fluvial incision and hill-slope rock flow. These processes are usually represented via a stream power law and a diffusive transport law, respectively [48,51,28]. For its simplicity and versatility, here we adopt the formulation developed by Beaumont et al. [13] and Kooi and Beaumont [52], which considers that a river has an intrinsic equilibrium transport capacity proportional to water discharge and slope along the topographic profile $z(x)$:

$$q^{\mathrm{eq}} = K_{\mathrm{f}} \cdot \left|\frac{\partial z}{\partial x}\right| \cdot Q_{\mathrm{w}} \tag{14}$$

where q^{eq} is the sediment transport capacity in equilibrium, K_{f} is the constant of fluvial transport capacity and Q_{w} is water discharge. The amount of river incision or aggradation at each location $e(x)$ is in turn proportional to the difference between the actual sediment load and the equilibrium transport capacity. Including the diffusive term, the total erosion is written as

$$e(x) = -\frac{1}{l_{\mathrm{f}}}\left(q(x) - q^{\mathrm{eq}}(x)\right) - K_{\mathrm{d}}\frac{\partial^2 z(x)}{\partial x^2} \tag{15}$$

where K_{d} is the constant of diffusive transport, q is the actual sediment load transferred from upstream tributary cells, and l_{f} is a constant determining how rapidly the river attains the equilibrium transport capacity, measured in distance units. Negative values of e in this equation (when $q^{\mathrm{eq}} > q$) correspond to aggradation of fluvial sediments. Deposition of the sediment load arriving to the sea or a lake is applied by taking $q^{\mathrm{eq}}=0$ in Eq. (15) and defining an effective distance of deposition of $l_{\mathrm{f}}=15$ km.

Though slope is zero in the outlet of a lake, and therefore outlet erosion corresponds only to the last (diffusive) term in the right side of Eq. (15), curvature at the outlet is enhanced by fluvial incision in the escarpment. This, together with the reduction of $W_{\mathrm{l}}(z_{\mathrm{l}})$ as the outlet is eroded Eq. (13), produces a feedback effect on the capture process and ensures that open lakes disappear by outlet erosion if not by sediment overfill.

A.4. Lithospheric flexural isostasy

The mass redistribution related to tectonic deformation, surface sediment transport and changes in water volume of lakes and sea are isostatically compensated via a 1D thin-plate flexural approach with laterally constant elastic thickness T_{e}. The expression used to calculate the flexural deflection $w(x)$ is (e.g., [46]):

$$\frac{\mathrm{d}^2}{\mathrm{d}x^2}\left(D(x)\frac{\mathrm{d}^2 w(x)}{\mathrm{d}x^2}\right) + F_x\frac{\mathrm{d}^2 w(x)}{\mathrm{d}x^2} + \rho_m g w(x) = q(x) \tag{16}$$

ρ_m is the density of the asthenosphere, F_x is the horizontal tectonic force, q is change in load resting on the lithospheric plate, as a result of tectonic and surface processes, and D is the plate rigidity, related to the equivalent elastic thickness T_{e} through the relation

$$D = \frac{E T_e^3}{12(1-\nu^2)} \tag{17}$$

where E is Young's modulus, and ν is Poisson's coefficient. We approach F_x as the vertical integral of the tectonic stress $\Delta\sigma_{xx}$ over the thickness of the flexural plate:

$$F_x = \int_0^{\mathrm{Te}} \Delta\sigma_{xx}\mathrm{d}z = \Delta\sigma_{xx} T_{\mathrm{e}} \tag{18}$$

Large T_{e} values imply a more rigid behavior of the lithosphere under mass redistribution, resulting in smaller amplitude and longer wavelength distribution of isostatic vertical movements. In contrast, small T_{e} values imply that erosional unloading and tectonic and sediment loading are locally compensated by vertical rebound and subsidence, respectively.

References

[1] S. Wdowinski, Y. Bock, The evolution of deformation and topography of high elevated plateaus 1. Model, numerical analysis, and general results, J. Geophys. Res. 99 (1994) 7103–7119.

[2] L. Royden, Coupling and decoupling of crust and mantle in convergent orogens; implications for strain partitioning in the crust, J. Geophys. Res., B 101 (1996) 17,679–17,705.

[3] O. Vanderhaeghe, S. Medvedev, P. Fullsack, C. Beaumont, R.A. Jamieson, Evolution of orogenic wedges and continental plateaux: insights from crustal thermal–mechanical models overlying subducting mantle lithosphere, Int. J. Geophys. 153 (2003) 27–51.

[4] L. Husson, Y. Ricard, Stress balance above subduction: application to the Andes, Earth Planet. Sci. Lett. 222 (2004) 1037–1050.

[5] S.V. Sobolev, A.Y. Babeyko, What drives orogeny in the Andes? Geology 33 (2005) 617–620.

[6] T. Vietor, O. Oncken, Controls on the shape and kinematics of the Central Andean plateau flanks: insights from numerical modeling, Earth Planet. Sci. Lett. 236 (2005) 814–827, doi:10.1016/j.epsl.2005.06.004.

[7] B.L. Isacks, Uplift of the Central Andean plateau and the bending of the Bolivian Orocline, J. Geophys. Res. 93 (1988) 13,841–13,854.

[8] P. Rochat, G. Herail, P. Baby, G. Mascle, Bilan crustal et controle de la dynamique erosive et sedimentaire sur les mecanismes de formation de l'Altiplano. Crustal balance and control of erosive and sedimentary processes on the formation of the Altiplano, C. R. Acad. Sci. II 328 (1999) 189–195.

[9] N. McQuarrie, P. DeCelles, Geometry and structural evolution of the Central Andean backthrust belt, Bolivia, Tectonics 20 (2001) 669–692.

[10] C.N. Garzione, P. Molnar, J.C. Libarkin, B.J. MacFadden, Rapid late Miocene rise of the Bolivian Altiplano: evidence for removal of mantle lithosphere, Earth Planet. Sci. Lett. 241 (2006) 543–556.

[11] S. Lamb, L. Hoke, Origin of the high plateau in the Central Andes, Bolivia, South America, Tectonics 16 (1997) 623–649.

[12] F. Métivier, Y. Gaudemer, P. Tapponnier, B. Meyer, Northeastward growth of the Tibet plateau deduced from balanced reconstruction of two depositional areas: the Qaidam and Hexi Corridor basins, China, Tectonics 17 (1998) 823–842.

[13] C. Beaumont, P. Fullsack, J. Hamilton, Erosion control of active compressional orogens, in: K.R. McClay (Ed.), Thrust Tectonics, Chapman and Hall, London, 1992, pp. 1–18.

[14] S.D. Willett, Orogeny and orography: the effects of erosion on the structure of mountain belts, J. Geophys. Res. 104 (B12) (1999) 28957–28981.

[15] I. Jiménez-Munt, D. Garcia-Castellanos, M. Fernàndez, Thin sheet modelling of lithospheric deformation and surface mass transport, Tectonophysics 407 (2005) 239–255, doi:10.1016/j.tecto.2005.08.015.

[16] G. Simpson, Modelling interactions between fold-thrust belt deformation, foreland flexure and surface mass transport, Basin Res. 18 (2006) 125–143, doi:10.1111/j.1365-2117.2006.00287.x.

[17] J.L. Mugnier, P. Baby, B. Colletta, P. Vinoue, P. Bale, P. Leturmy, Thrust geometry controlled by erosion and sedimentation: a view from analogue models, Geology 25 (1997) 427–430.

[18] K.S. Persson, D. Garcia-Castellanos, D. Sokoutis, River transport effects on compressional belts: first results from an integrated analogue-numerical model, J. Geophys. Res. 109 (B1) (2004) B01409, doi:10.1029/2002JB002274.

[19] F. Schlunegger, G. Simpson, Possible erosional control on lateral growth of the European Central Alps, Geology 30 (2002) 907–910, doi:10.1130/0091-7613.

[20] E.R. Sobel, G.E. Hilley, M. Strecker, Formation of internally-drained contractional basins by aridity-limited bedrock incision, J. Geophys. Res. 108 (2003) 7 (25 pp.).

[21] D. Garcia-Castellanos, J. Verges, J.M. Gaspar-Escribano, S. Cloetingh, Interplay between tectonics, climate and fluvial transport during the Cenozoic evolution of the Ebro Basin (NE Iberia), J. Geophys. Res. 108 (2003) 2347, doi:10.1029/2002JB002073.

[22] D. Garcia-Castellanos, Long-term evolution of tectonic lakes: climatic controls on the development of internally drained basins, in: S.D. Willett, N. Hovius, M.T. Brandon, D.M. Fisher (Eds.), Tectonics, Climate, and Landscape Evolution, GSA Special Paper, vol. 398, 2006, pp. 283–294, doi:10.1130/2006.2398(17).

[23] J.G. Masek, B.L. Isacks, T.L. Gubbels, E.J. Fielding, Erosion and tectonics at the margins of continental plateaus, J. Geophys. Res. 99 (1994) 13941–13956.

[24] R.A. Carroll, K.M. Bohacs, Stratigraphic classification of ancient lakes: balancing tectonic and climatic controls, Geology 27 (1999) 99–102.

[25] D.W. Burbank, The chronology of intermontane-basin development in the northwestern Himalaya and the evolution of the Northwest Syntaxis, Earth Planet. Sci. Lett. 64 (1983) 77–92.

[26] R.P. Irwin, T.A. Maxwell, A.D. Howard, R.A. Craddock, D.W. Leverington, A large paleolake basin at the head of Ma'adim-Vallis, Mars, Science 296 (2002) 2209–2212.

[27] D. Garcia-Castellanos, M. Fernàndez, M. Torné, Numerical modeling of foreland basin formation: a program relating thrusting, flexure, sediment geometry and lithosphere rheology, Comput. Geosci. 23 (1997) 993–1003.

[28] K.X. Whipple, G.E. Tucker, Dynamics of the stream-power river incision model; implications for height limits of mountain ranges, landscape response timescales, and research needs, J. Geophys. Res., B, Solid Earth Planets 104 (8) (1999) 17,661–17,674.

[29] P. van der Beek, J. Braun, Controls on post-Mid-Cretaceous landscape evolution in the southeastern highlands of Australia; insights from numerical surface process models, J. Geophys. Res., B 104 (3) (1999) 4945–4966.

[30] L.S. Sklar, W.E. Dietrich, Sediment and rock strength controls on river incision into bedrock, Geology 29 (2001) 1087–1090.

[31] A. Tassara, C. Swain, R. Hackney, J. Kirby, Elastic thickness structure of South America estimated using wavelets and satellite-derived gravity data, Earth Planet. Sci. Lett. 253 (2006) 17–36, doi:10.1016/j.epsl.2006.10.008.

[32] G.D. Karner, A.B. Watts, Gravity anomalies and flexure of the lithosphere at mountain ranges, J. Geophys. Res. 88 (1983) 10449–10477.

[33] J. Steward, A.B. Watts, Gravity anomalies and spatial variations of flexural rigidity at mountain ranges, J. Geophys. Res. 102 (B3) (1997) 5327–5352.

[34] I. Jimenez-Munt, D. Garcia-Castellanos, A. Negredo, J. Platt, Gravitational and tectonic forces controlling the post-collisional deformation and present-day stress of the Alps. Insights from numerical modelling, Tectonics 24 (2005), doi:10.1029/2004TC001754.

[35] D. Pope, S.D. Willett, A thermo-mechanical model for the formation of the Central Andes-Altiplano of South America, Geology 26 (1998) 511–514.

[36] S. Lamb, P. Davis, Cenozoic climate change as a possible cause for the rise of the Andes, Nature (Lond.) 425 (2003) 792–797.

[37] C.W. Fuller, S. Willett, M.T. Brandon, Formation of forearc basins and their influence on subduction zone earthquakes, Geology 34 (2006) 65–68, doi:10.1130/G21828.1.

[38] P. Molnar, H. Lyon-Caen, Some simple physical aspects of the support, structure, and evolution of mountain belts, Processes in Continental Lithospheric Deformation, Special Paper of the Geological Society of America, vol. 218, 1988, pp. 179–207.
[39] T.J. Dunai, G.A Gonzalez Lopez, J. Juez-Larre, Oligocene–Miocene age of aridity in the Atacama Desert revealed by exposure dating of erosion-sensitive landforms, Geology (Boulder) 33 (2005) 321–324.
[40] A.J. Hartley, G. Chong, J. Houston, E. Anne Mather, 150 million years of climatic stability: evidence from the Atacama Desert, northern Chile, J. Geol. Soc. (Lond.) 162 (2005) 421–424.
[41] J.A. Rech, B.S. Currie, G. Michalski, A.M. Cowan, Neogene climate change and uplift in the Atacama Desert, Chile, Geology 34 (2006) 761–764.
[42] B. Kraemer, D. Adelmann, M. Alten, W. Schnurr, K. Erpenstein, E. Kiefer, P. van den Bogaard, K. Görler, Incorporation of the Paleogene foreland into Neogene Puna plateau: the Salar de Antofolla, NW Argentina, J. South Am. Earth Sci. 12 (1999) 157–182.
[43] B. Carrapa, D. Adelmann, G.E. Hilley, E. Mortimer, E.R. Sobel, M.R. Strecker, Oligocene range uplift and development of plateau morphology in the southern central Andes, Tectonics 24 (2005), doi:10.1029/2004TC001762.
[44] P.G. DeCelles, B.K. Horton, Early to middle Tertiary foreland basin development and the history of Andean crustal shortening in Bolivia, Geol. Soc. Amer. Bull. 115 (2003) 58–77.
[45] J.G. Masek, C.C. Duncan, Minimum-work mountain building, J. Geophys. Res. 103 (1998) 907–917.
[46] D.L. Turcotte, G. Schubert, Geodynamics, Cambridge University Press, Cambridge, United Kingdom, 2002, 456 pp.
[47] R.S. Purves, N.R.J. Hulton, A climatic-scale precipitation model compared with the UKCIP baseline climate, Int. J. Climatol. 20 (14) (2000) 1809–1821.
[48] A.D. Howard, A detachment-limited model of drainage basin evolution, Water Resour. Res. 30 (1994) 2261–2285.
[49] A. Kühni, O.A. Pfiffner, Drainage patterns and tectonic forcing: a model study for the Swiss Alps, Basin Res. 13 (2) (2001) 169–197.
[50] P. van der Beek, B. Champel, J.-L. Mugnier, Control of detachment dip on drainage development in regions of active fault-propagation folding, Geology 30 (2002) 471–474.
[51] G.E. Tucker, R.L. Slingerland, Drainage responses to climate change, Water Resour. Res. 33 (8) (1997) 2031–2047.
[52] H. Kooi, C. Beaumont, Escarpment retreat on high-elevation rifted continental margins: insights derived from a surface process model that combines diffusion, reaction, and advection, J. Geophys. Res. 99 (1994) 12191–12202.
[53] G. Wörner, D. Uhlig, I. Kohler, H. Seyfried, Evolution of the West Andean Escarpment at 18 S (N. Chile) during the last 25 Ma: uplift, erosion and collapse through time, Tectonophysics 345 (2002) 183–198.
[54] F. Kober, F. Schlunegger, R. Wieler, S. Ivy-Ochs, G. Simpson, Determination of erosion rates in a decoupled river and pediplane system in the central Andes, northern Chile, Proceedings of the 5th International Symposium on Andean Geodynamics (ISAG), Toulouse, Sept. 2002.
[55] C.N. Alpers, G.H. Brimhall, Middle Miocene climate change in the Atacama Desert, northern Chile. Evidence from supergene mineralization at La Escondida, GSA Bull. 100 (1988) 1640–1656.
[56] J.I. Garver, P.W. Reiners, L.J. Walker, J.M. Ramage, S.E. Perry, Implications for timing of Andean uplift from thermal resetting of radiation-damaged zircon in the Cordillera Huayhuash, northern Peru, J. Geol. 113 (2005) 117–138.
[57] Ege, H., 2004. Exhumations- und Hebungsgeschichte der zentralen Anden in Südbolivien (21°S) durch Spaltspur-Thermochronologie an Apatit, Ph.D. thesis, 159 pp., Freie Universität Berlin, Germany.
[58] S.T. Crough, Apatite fission-track dating of erosion in the eastern Andes, Bolivia, Earth Planet. Sci. Lett. 64 (1983) 396–397.
[59] E.B Safran, P.R. Bierman, R. Aalto, T. Dunne, K.X. Whipple, M.W. Caffee, Erosion rates driven by channel network incision in the Bolivian Andes, Earth Surf. Processes and Landf. 30 (2005) 1007–1024.
[60] G.H. Roe, D.R. Montgomery, B. Hallet, Orographic precipitation and the relief of mountain ranges, J. Geophys. Res. 108 (2003) 2315, doi:10.1029/2001JB001521.